III. MEASUREMENT OF PHASE FRACTIONS BY GAMMA–RAY DENSITOMETRY

In many applications of industrial importance, systems operate at high temperatures and pressures. Under these conditions, experimental techniques commonly employed in hydrodynamic studies with systems that operate at low temperatures and pressures may not be applicable. Gamma–ray densitometry in a non–intrusive technique which may be used to measure various hydrodynamic parameters at high temperatures and pressures. The majority of previous investigations which have utilized this technique were limited to two–phase systems. Recently, several investigators (Seo and Gidaspow, 1987; Bernatowicz et al., 1987; and Abouelwafa and Kendall, 1980) have successfully used this technique to measure phase fractions in three–phase systems. However, the thickness of the absorbing media was less than 0.03 m. The objective of this work was to design and construct a dual energy gamma–ray densitometer which could be used to measure volume fractions (gas/liquid/solids) in a large diameter (0.21 m ID) bubble column.

Experiments were conducted using both two–phase and three–phase systems (see Table 2.5). Volume fractions were measured with a dual energy gamma–ray densitometer during most of these experiments. The theory associated with gamma–ray absorption, the selection of sources, the experimental apparatus and calibration techniques used, the applicability of this technique to large diameter three–phase systems and results from experiments conducted in both two–phase and three–phase systems will be discussed.

Theoretical Discussion

Gamma–ray absorption is based on the fact that the intensity of radiation decreases as it passes through a material. The change in intensity, ΔI, is proportional to the

thickness of the material, Δx, and the incident intensity, I_o. Therefore,

$$\Delta I = -\mu I_o \Delta x \tag{3.1}$$

where μ is a proportionality constant called the mass attenuation coefficient. If the radiation is homogeneous, Eq. 3.1 may be written as:

$$dI = -\mu I_o dx \tag{3.2}$$

which upon integration yields:

$$I = I_o \exp(-\mu x) \tag{3.3}$$

The intensity of radiation is given by:

$$I = h\nu B \tag{3.4}$$

where $h\nu$ is the energy/photon, B_o is the incident number (i.e. no absorber) of photons crossing a unit area per unit time, and B is the number of uncollided photons crossir a unit area per unit time. Thus, Eq. 3.3 may be written in terms of the number of photons or counts per second,

$$B = B_o \exp(-\mu x) \tag{3.5}$$

As discussed by Attix (1968), attenuation of the energy of an incident photon may occur through both scattering and absorption of the photon. Attenuation by some purely elastic process in which a photon does not give up any of its initial energy to the medium, but is merely deflected, is called scattering (e.g. Raleigh scattering). Whereas, in absorption, the entire energy of the incident photon is absorbed. One type of absorption process is called the photoelectric effect. During this process, the entire energy of an incident photon is absorbed by an atom of the medium and an electron is emitted. Pair–production, is another process by which total absorption may occur. During pair–production, a photon may be totally absorbed in either the atomic nucleus

or the field of an atomic electron, and a positron–negatron pair is emitted. The Compton effect is the intermediate case, in which some of the energy of the incident photon is absorbed and appears as a Compton recoil electron, and the remaining incident energy is present as a Compton scattered electron. The attenuation process includes both scattering and absorption of the incident photon. Thus, the attenuation coefficient, μ is the sum of the absorption coefficients, μ_a and the scattering coefficients, μ_s.

For energies in the range 0.01 to 10 MeV, attenuation is due primarily to photoelectric interactions, Compton scattering and absorption, and pair–production. Figure 3.1 (from Evans, 1955), shows the energy ranges over which these competing effects dominate for various atomic numbers, Z. For relatively large values of Z, the photoelectric effect dominates at low energies and pair–production dominates at high energies.

Attix (1968) present interpolation formulas which may be used to estimate attenuation coefficients for compounds given attenuation coefficients for the elements comprising the compounds. They also give formulas for estimating absorption and scattering coefficients for elements for which experimental data are not available. The following formula may be used to estimate the attenuation coefficient, μ_{mix}, for a compound

$$\frac{\mu_{mix}}{\rho_{mix}} = \sum_i \frac{\mu_i}{\rho_i}\omega_i \qquad i = 1 \text{ to no. of components} \tag{3.6}$$

where μ_i is in cm^{-1} and ω_i is the weight fraction of component i. The following interpolation formula may be used to estimate either Compton absorption or Compton scattering coefficients, σ_i

$$\frac{\sigma_1}{\rho_1} = \left(\frac{\sigma_2}{\rho_2}\right)\left(\frac{A_2}{A_1}\right)\left(\frac{Z_1}{Z_2}\right) \tag{3.7}$$

where Z is the atomic number, A is the atomic mass, and the subsripts 1 and 2 represent any two elements. For the photoelectric effect, the interpolation formula for the absorption coefficient , τ_i, is

$$\frac{\tau_1}{\rho_1} = \left(\frac{\tau_2}{\rho_2}\right)\left(\frac{A_2}{A_1}\right)\left(\frac{Z_1}{Z_2}\right)^n \tag{3.8}$$

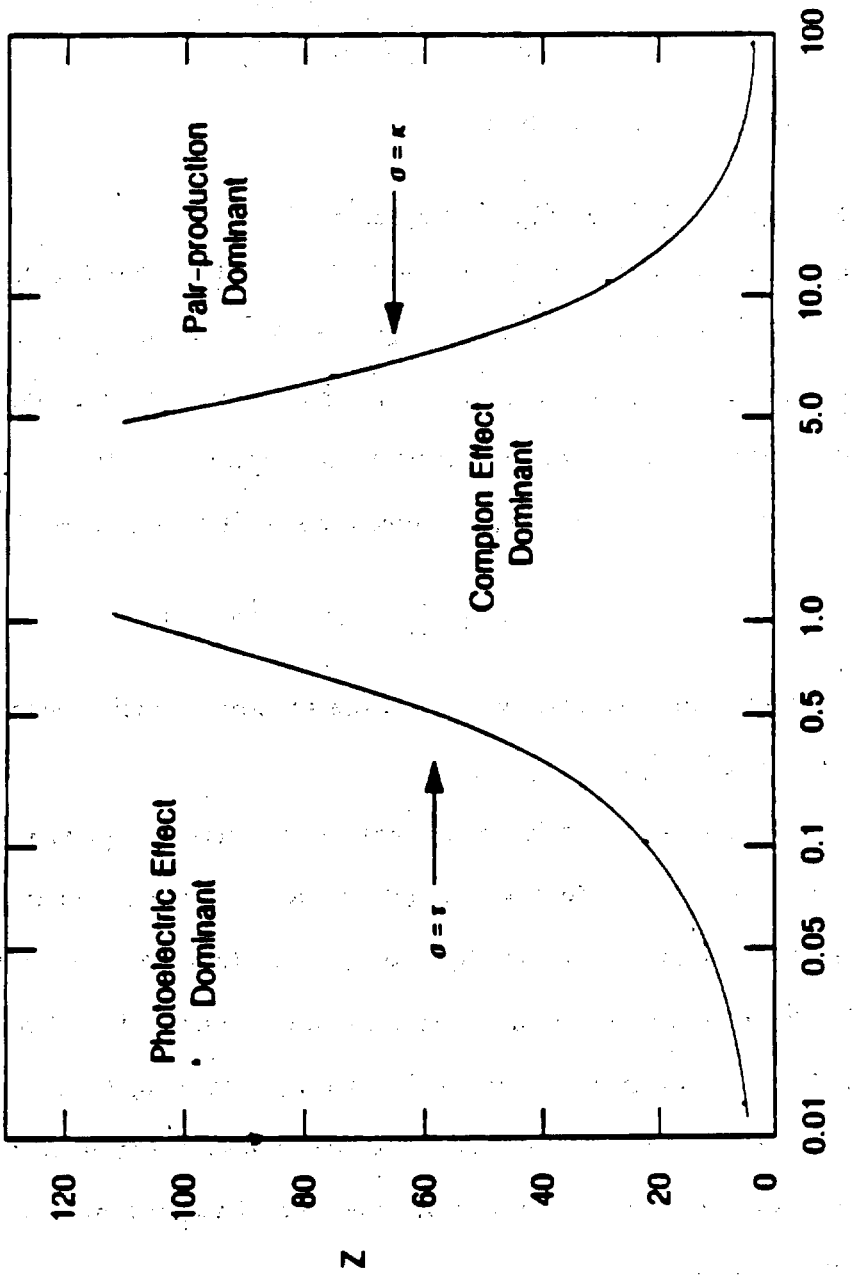

Figure 3.1. Relative importance of the three major types of gamma-ray attenuation.

where the exponent n is a function of the energy of the incident photon and ranges from 4 to 4.6. And, for pair–production,

$$\frac{\kappa_1}{\rho_1} = \left(\frac{\kappa_2}{\rho_2}\right)\left(\frac{A_2}{A_1}\right)\left(\frac{Z_1}{Z_2}\right)^2 \tag{3.9}$$

where κ_i is the absorption coefficient.

Models Used to Describe Three – Phase Systems

When the photons emitted from a radioactive source pass though a homogeneous material, a fraction of the energy associated with the photons is attenuated and Eq. 3.5 describes the absorption process. If multiple absorption mediums are aligned perpendicular to the incident beam of radiation (see Figure 3.2), the number of uncollided photons passing through the absorbing media per unit time is given by:

$$B = B_o \exp(-\sum_i \mu_i x_i) \qquad i = 1 \text{ to } n \tag{3.10}$$

where x_i is the thickness of absorber i; μ_i is the absorption coefficient for medium i; and n is the number of different absorbers.

In a three–phase bubble column, the gas, solid, and liquid phases are the absorbing media. The model used to describe the interaction between the beam of radiation and the three phases depends on the alignment of the three phases with respect to the beam of radiation. Two types of orientations were examined in this research. In one case, the three phases were assumed to be aligned perpendicular to the incident beam of radiation, and for the other case, all three phases were assumed to be aligned parallel to the beam of radiation. The two cases mentioned above represent the extremes of possible alignments.

Case I. Perpendicular Alignment

For the first case (i.e. perpendicular alignment), we assume that the beam of radiation may be represented by a cylinder, with the three phases occupying slices of

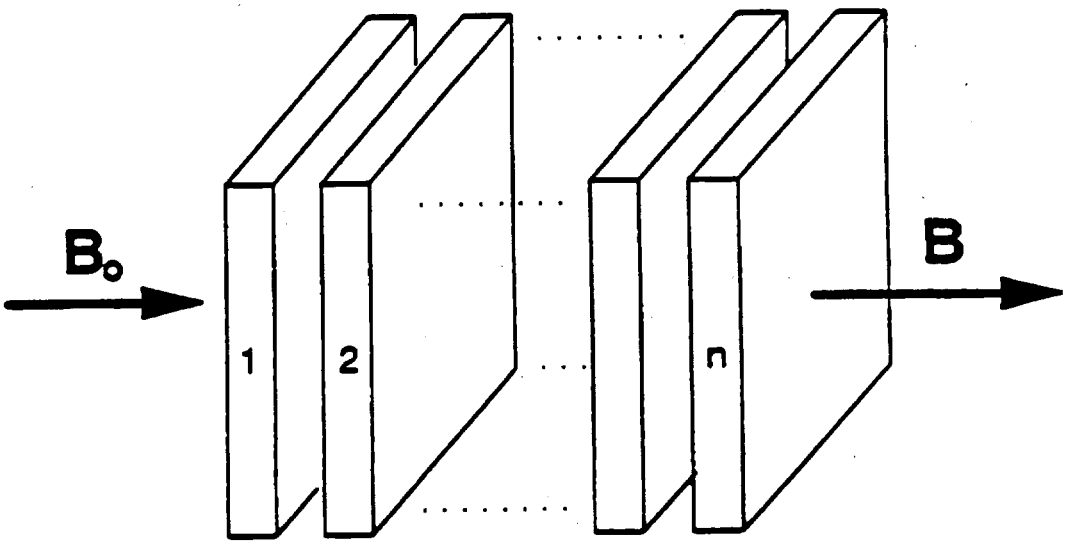

Figure 3.2. Schematic representation of multiple absorbers in series.

the cylinder (Figure 3.3). For this alignment, Eq. 3.10 may be used to describe the absorption process. The volume of phase i through which the beam of radiation passes is given by:

$$V_i = x_i A_x \qquad i = g, \ell, s \tag{3.11}$$

where A_x is the cross–sectional area of the absorbing media. The total volume of the absorbing media is

$$V_t = dA_x \tag{3.12}$$

The volume fraction of phase i, ϵ_i, is defined as the volume of phase i (Eq. 3.11) divided by the total volume (Eq. 3.12) and may be expressed as:

$$\epsilon_i = \frac{x_i A_x}{dA_x} \qquad i = g, \ell, s \tag{3.13}$$

or, the thickness of the absorbing media, x_i is

$$x_i = d\epsilon_i \qquad i = g, \ell, s \tag{3.14}$$

Substituting Eq. 3.14 into Eq. 3.10 for x_i yields the following expression for the amount of radiation transmitted through the column

$$B = B_o \exp[-d(\mu_g \epsilon_g + \mu_\ell \epsilon_\ell + \mu_s \epsilon_s)] \tag{3.15}$$

where the subscripts g, ℓ, and s refer to the gas, liquid, and solid phases, respectively. Equation 3.15 contains three unknowns, i.e. the volume fractions of the three phases. Thus, two additional equations are needed to characterize the system. Since attenuation coefficients are a function of radioactive source strength (i.e. energy), another equation arises from the use of an additional source. This equation is identical to Eq. 3.15 except that the values of the attenuation coefficients are different. These two equations along with a volume balance are used to obtain volume fractions of the individual phases.

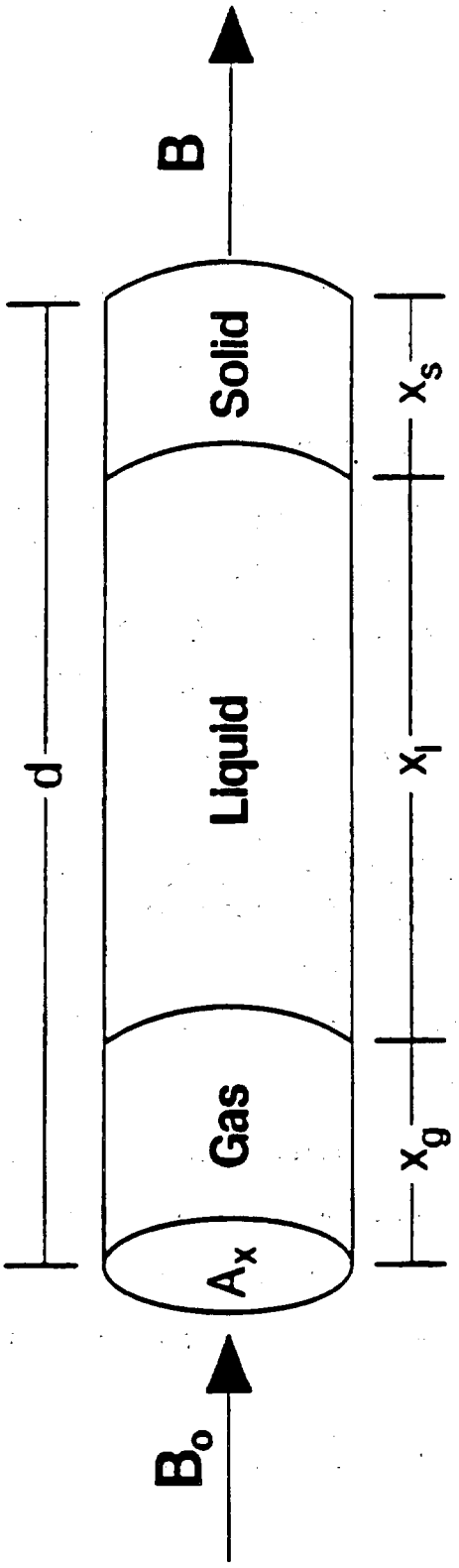

Figure 3.3. Schematic representation of Case I geometry (i.e. perpendicular alignment).

Thus, the set of equations used to determine volume fractions in a three–phase system is:

$$B_1 = B_{o1}\exp[-d(\mu_{g1}\epsilon_g + \mu_{\ell 1}\epsilon_\ell + \mu_{s1}\epsilon_s)] \tag{3.16}$$

$$B_2 = B_{o2}\exp[-d(\mu_{g2}\epsilon_g + \mu_{\ell 2}\epsilon_\ell + \mu_{s2}\epsilon_s)] \tag{3.17}$$

$$1 = \epsilon_g + \epsilon_\ell + \epsilon_s \tag{3.18}$$

where the subscripts 1 and 2 refer to the two different radioactive sources.

At atmospheric pressure, the attenuation of radiation due to the gas phase phase is negligible, and the quantity $\mu_{gi}\epsilon_{gi}$ may be omitted from equations 3.16 and 3.18. If the absorption by the gas phase is neglected, Eqs. 3.16 and 3.17 may be combined to yield a single expression for either the volume fraction of solids or the volume fraction of liquid. The volume fraction of the liquid phase is

$$\epsilon_\ell = \frac{\ln(B_1 / B_{o1})\mu_{s2} + \ln(B_2 / B_{o2})\mu_{s1}}{d(\mu_{\ell 2}\mu_{s1} - \mu_{\ell 1}\mu_{s2})} \tag{3.19}$$

Once the value of ϵ_ℓ is known, it is substituted into either Eq. 3.16 or Eq. 3.17 to obtain a value for ϵ_s. The gas holdup is then calculated from Eq. 3.18.

Case II. Parallel Alignment

Another possible geometric relationship between the incident beam of radiation and the absorbing media is when the three phases are aligned in parallel with respect to the beam of radiation (see Figure 3.4). A fraction of the incident beam of radiation passes through each phase separately. The fraction of the incident beam passing through a given phase is

$$f_{o_i} = \frac{A_i}{A_x} = \epsilon_i \qquad i = g, \ell, s \tag{3.20}$$

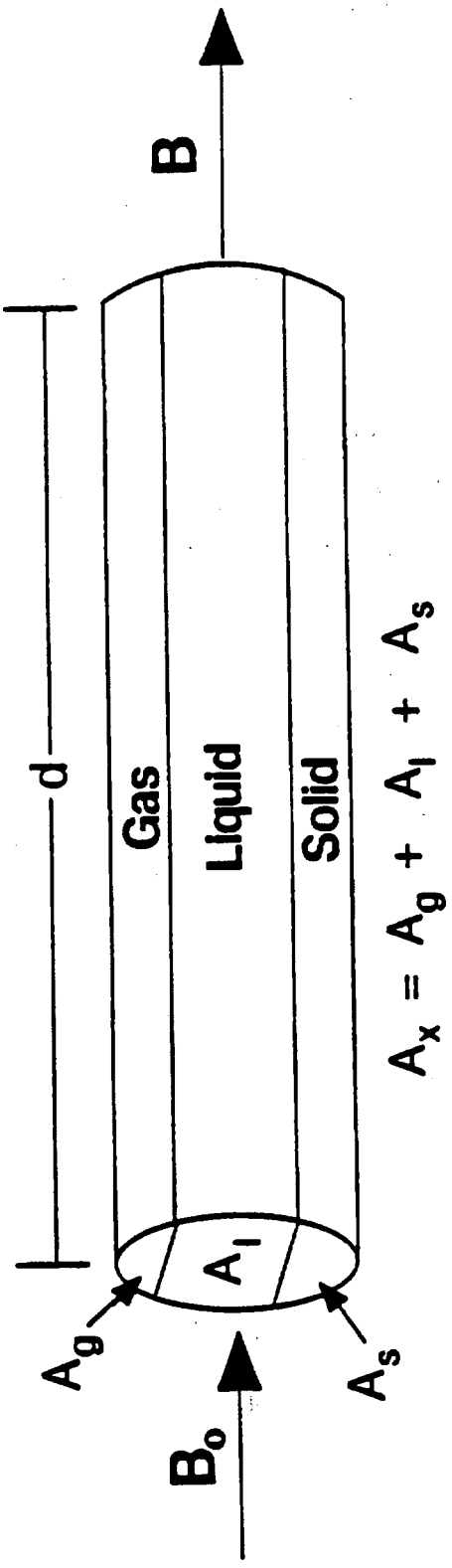

Figure 3.4. Schematic representation of Case II geometry (i.e. parallel alignment).

where A_i is the cross-sectional area of the cylinder occupied by the i^{th} phase. Thus, the amount of radiation passing through a given phase is

$$B_i = B_o \epsilon_i \exp(-\mu_i d) \qquad i = g, \ell, s \tag{3.21}$$

The total amount of radiation which passes through the absorbing media is the sum of the amounts of radiation which passes through the three phases,

$$B = B_o[\epsilon_g \exp(-d\mu_g) + \epsilon_\ell \exp(-d\mu_\ell) + \epsilon_s \exp(-d\mu_s)] \tag{3.22}$$

Once again, two different radioactive sources are needed and we may assume that attenuation due to the gas phase is negligible. The final set of equations used to describe this type of configuration is:

$$B_1 = B_{o1}[\epsilon_g + \epsilon_\ell \exp(-d\mu_{\ell 1}) + \epsilon_s \exp(-d\mu_{s1})] \tag{3.23}$$

$$B_2 = B_{o2}[\epsilon_g + \epsilon_\ell \exp(-d\mu_{\ell 2}) + \epsilon_s \exp(-d\mu_{s2})] \tag{3.24}$$

$$1 = \epsilon_g + \epsilon_\ell + \epsilon_s \tag{3.25}$$

Equations 3.23 to 3.25 may be solved to obtain the following expression for ϵ_ℓ,

$$\epsilon_\ell = \frac{(B_1 / B_{o1}) - 1 - \frac{((B_2/B_{o2})-1)(\exp(-d\mu_{s1})-1)}{(\exp(-d\mu_{s2})-1)}}{(\exp(-d\mu_{\ell 1}) - 1) - \frac{(\exp(-d\mu_{\ell 2})-1)(\exp(-d\mu_{s1})-1)}{\exp(-d\mu_{s2})-1}} \tag{3.26}$$

Equation 3.25 may be substituted into either Eq. 3.23 or Eq. 3.24 to obtain an expression for ϵ_s in terms of ϵ_ℓ. If Eq. 3.24 is used, the expression for ϵ_s is

$$\epsilon_s = \frac{(B / B_{o2}) - 1 - \epsilon_\ell(\exp(-d\mu_{\ell 2}) - 1)}{\exp(-d\mu_{s2}) - 1} \tag{3.27}$$

The value of ϵ_ℓ calculated from Eq. 3.26 is substituted into Eq. 3.27 to obtain a value for ϵ_s. Using these two values, the gas holdup, ϵ_g, is calculated directly from Eq. 3.25.

Comments on the Alignment of the Phases

Actual phase alignment with respect to the beam of radiation for two and three-phase flow will lie between the two cases described above. However, since there is a considerable amount of homogeneity in the flow patterns (except in the slug flow regime) in bubble columns, it may be assumed that the majority of the radiation will be attenuated according to Case I alignment.

Previous studies with three-phase systems (e.g. Bernatowicz et al., 1987; Seo and Gidaspow, 1987; Abouelwafa and Kendall, 1980) used Case I alignment (i.e. phases perpendicular to incident beam of radiation) to model the attenuation process. Petrick (1958) constructed several lucite models representative of different types of flow patterns in a two-phase system. There was excellent agreement between the predicted volume fractions and the actual volume fractions (< 7% relative error) assuming Case I alignment. In his experiments, he measured the volume fractions at various radial locations and used the average value. He also measured the volume fraction at a single location (i.e "one shot" method), and the error between the actual and predicted volume fractions was considerably higher (< 36% relative error) for models representative of non-homogeneous flow conditions. Under actual two-phase flow conditions in a vertical tube (air-water system), Petrick showed that when the width of the beam of radiation was equal to the width of the absorbing medium (i.e. the column diameter), there was no difference between volume fractions predicted using several measurements and averaging the results, and volume fractions obtained using the "one shot" method. However, when the column diameter was increased such that the width of the beam of radiation was less than the column diameter, he observed differences in the volume fraction calculated using the two techniques. He attributed the differences in results, to differences in the radial distribution of the volume fractions of air and water. Thus,

not only phase alignment, but also phase distributions (i.e. axial and radial variations in phase fractions) need to be taken into account when using the gamma–ray technique.

Figures 3.5a and 3.5b are schematic representations of two possible phase distributions (two–phases) in a square channel. Figure 3.5a represents annular flow, in which a gas fills the center of the duct, and Figure 3.5b, represents homogeneous flow (i.e. no radial variation in volume fractions). Based on the dimensionless distances given in Figure 3.5, the actual volume fraction of gas is 0.25 for both cases. For homogeneous flow conditions (Figure 3.5b), regardless of the radial location of the measurement, the volume fraction of gas (or liquid) may be accurately determined at any location assuming Case I alignment (i.e. using Eq. 3.10). However, for annular flow, if a single measurement is made in the center of the duct (see section A in Figure 3.5a), the measured volume fraction of gas obtained assuming Case I alignment would be 0.5 as opposed to the actual value of 0.25. Phase alignment becomes a problem, if measurements are made through section B in Figure 3.5a. In order to overcome these problems, measurements should be made at various locations across the duct and the volume fractions obtained from each measurement (via Eq. 3.10) should be averaged over the entire cross section of the duct to obtain an accurate estimate of the phase fractions.

Source Selection and Sensitivity Analysis

A gamma–ray densitometer system consists of three main parts: (1) radioactive sources, (2) detectors, and (3) associated electronic equipment. Of the three main components, the sources are the most important.

One must consider several factors, when selecting sources. These include transmission through the pipe walls and sensitivity to the slurry content. These two factors are competing. The lower the gamma–ray energy (i.e. higher attenuation) the more sensitive the system is to changes in the volume fractions of the slurry; however, with a

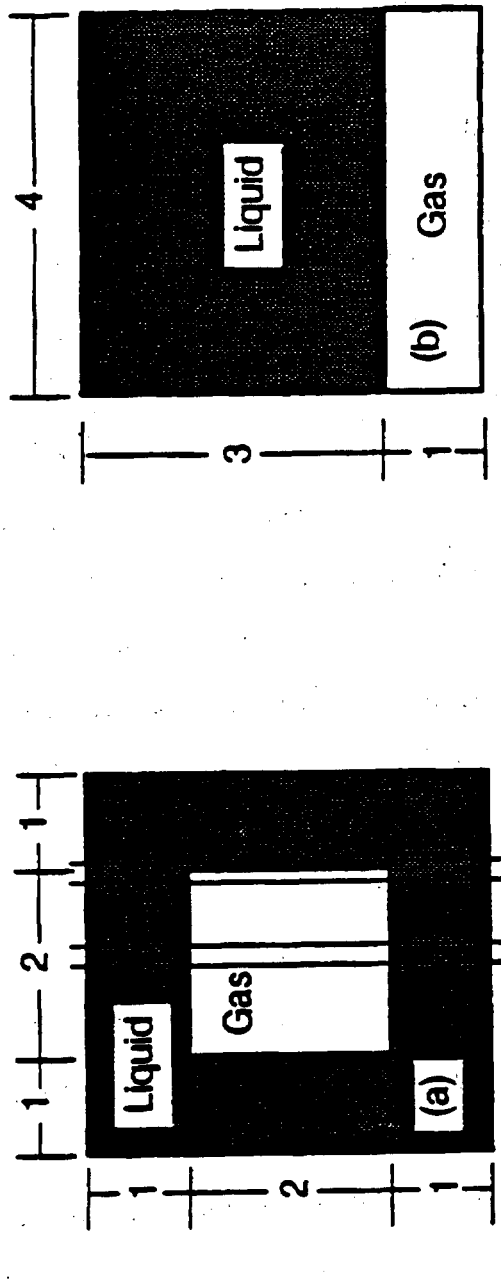

Figure 3.5. Schematic representations of (a) annular flow and (b) homogeneous flow in a square duct.

low energy source, more of the photons emitted from the source are attenuated by the vessel walls. This becomes a significant factor when the vessels (i.e. bubble column in this case) have thick metal walls. Other factors which need to be considered are the half–life of the source and the availability of the source. If a source with a very short half–life is used, then calibrations of the empty test section will have to be repeated frequently. This is to ensure that the initial count rate (or count rate through the empty pipe, B_o) is correct.

The factors described above need to be considered when selecting sources for both two–phase and three–phase applications. However, when two sources are required (i.e. three–phase measurements) one other criterion must be taken into account. Abouel-wafa and Kendall (1980) contend that the gamma–ray technique may be applied to multiphase systems provided the attenuation coefficients for the various phases are "different" for the sources selected. However, they never quantify what is meant by "different". It is obvious from Eqs. 3.16 and 3.17 that the attenuation coefficients for each phase must be "different" for the equations to be independent. However, it should be pointed out that while this is true, the following restriction must also be applied

$$\left(\frac{\mu_{\ell_1}}{\mu_{s_1}}\right)\left(\frac{\mu_{s_2}}{\mu_{\ell_2}}\right) \neq 1 \qquad (3.28)$$

If the above criterion is not satisfied, the denominator in Eq. 3.19 is zero and volume fractions cannot be calculated. This poses a serious problem when the gamma–ray technique is applied to large diameter systems. As discussed previously, attenuation is due primarily to the photoelectric effect, Compton scattering and absorption, and pair production. Furthermore the various types of attenuations (i.e. photoelectric, Compton, and pair production) dominate at certain energy levels as shown in Figure 3.1. If two different sources are selected, with different attenuation coefficients; however, if attenuation is dominated by the same process for both sources, the denominator in

Eq. 3.19 approaches 0.0 making the calculated value of ϵ_ℓ very sensitive to slight errors in the measured quantities (i.e. count rates). It follows from Eqs. 3.6 to 3.9 that the best results would be obtained if a low energy source (i.e. one in which attenuation was dominated by the photoelectric effect) and a relatively high energy source (i.e. one in which attenuation was dominated by Compton scattering and absorption) were used.

However, in a large diameter system, it may not be possible to use a low energy source since the majority of the radiation will be attenuated by the absorbing medium. Thus, it is necessary to use a higher energy source. If this is the case, then the second source would have to be extremely powerful (i.e. energy $>$ 10 MeV) to satisfy the criterion presented in Eq. 3.28. However, these sources pose serious safety problems and may not be readily available.

Nevertheless, for a given set of two sources, the appropriate source activity must be chosen. The activity required will depend on several factors, including the counting period, collimation diameter, length of the collimator, detector efficiency, and emission ratio of the desired gamma-rays (Chan and Banerjee, 1981).

It is well known that the counting process is a Poisson process, where the probability of n counts occurring in the time interval Δt is given by:

$$P_n = \frac{(B\Delta t)^n}{n!}\exp(B\Delta t) \tag{3.29}$$

The mean and variance of the Poisson process is B (i.e. the count rate). The standard deviation is $\sqrt{B}$. Thus, the actual count rate is the measured count rate $\pm \sqrt{B}$. Hence, the uncertainty in the count rate is $\frac{\sqrt{B}}{B}$. If B_o (i.e. empty column count rate) is measured over an extended period of time, the statistical error in B_o is assumed to be insignificantly small and the statistical error in void fractions may be calculated assuming only errors (or uncertainty) in the measured count rates (i.e. B).

Commercially available sources, with energies ranging from 0.0595 MeV (Americium – 241) to 1.17,1.33 MeV (Cobalt–60) were used to simulate the effect of uncertainty in the count rate on the predicted phase fractions. The two source combinations used to study the effect of errors in count rate on phase fractions were: (1) Americium – 241 – Cobalt–60 and (2) Cesium–137 (0.661 MeV) – Cobalt–60. For these simulations, the liquid phase was assumed to be a straight chain (C52) paraffin wax (MW = 730), and the solid phase was iron oxide. For the purpose of these calculations, Case 1 alignment was used, and the attenuation due to the gas phase was assumed negligible.

The attenuation coefficients for the solid and liquid phases for each source were estimated from data presented by Attix (1968). Attenuation coefficients are given by Attix for elements with atomic numbers up to 28 for energies ranging from 0.01 to 10 MeV. Equation 3.6 was used to estimate the attenuation coefficients for iron oxide and wax. Table 3.1 lists the attenuation coefficients used for sensitivity analysis. The criterion established in Eq. 3.28 is satisfied for both source combinations. For the Americium–Cobalt system, the quantity on the left hand side of Eq. 3.28 is 0.2, and for the Cesium–Cobalt system, the quantity on the left hand side of Eq. 3.28 is 0.98. Thus, one would expect that slight errors in measured quantities (i.e. count rates) would have less of an effect on the predicted volume fractions for the Americium–Cobalt system as compared to the Cesium–Cobalt system.

Tables 3.2a and 3.2b show results for the Americium–Cobalt system for errors in the count rate of Cobalt and errors in the count rate of Americium, respectively. An error of 1% in the Cobalt count rate corresponds to an error of approximately 10% in the predicted gas holdup. However, an error of 10 % in the Americium count rate would produce an error of only 4.5 % in the predicted gas holdup. Tables 3.3a and 3.3b show results for the Cesium–Cobalt system. For this system, an error of only 0.1 % in the count rates of Cesium or Cobalt produces an error of 19% and 26%, respectively, in the

Table 3.1. Attenuation Coefficients (cm^{-1}) Used for Error Analysis Calculations

ABSORBING MEDIUM	SOURCE		
	Am–241	Co–60	Cs–137
WAX ($C_{52}H_{106}$)	0.139	0.0423	0.0580
IRON OXIDE	4.575	0.2710	0.3820

Table 3.2a. Effect of Errors in the Count Rate of Co–60 on Volume Fractions Using the Am–241 and Co–60 System

% ERROR IN COUNT RATE	ϵ_g	% error	ϵ_s	% error
+0.1	0.152	1.3	0.0300	–
+0.5	0.157	4.7	0.0302	0.7
+1.0	0.165	10.0	0.0305	1.7
+5.0	0.223	48.7	0.0320	6.7
+10.0	0.294	96.0	0.0340	13.3

Table 3.2b. Effect of Errors in the Count Rate of Am–241 on Volume Fractions Using the Am–241 and Co–60 System

% ERROR IN COUNT RATE	ϵ_g	% error	ϵ_s	% error
+0.1	0.1500	–	0.0300	–
+0.5	0.1496	0.27	0.0299	0.3
+1.0	0.1492	0.5	0.0305	0.7
+5.0	0.1462	2.5	0.0320	2.3
+10.0	0.1426	4.9	0.0286	4.7

Base Conditions: $\epsilon_g = 0.15$, $\epsilon_\ell = 0.82$, and $\epsilon_s = 0.03$

Table 3.3a. Effect of Errors in the Count Rate of Co–60 on Volume Fractions Using the Cs–137 and Co–60 System

% ERROR IN COUNTRATE	ϵ_g	% error	ϵ_s	% error
+0.1	0.189	26	0.037	23
+0.5	0.344	129	0.065	117
+1.0	0.537	258	0.099	230
+5.0	2.050	1267	0.370	1133
+10.0	3.860	2473	0.694	2213

Table 3.3b. Effect of Errors in the Count Rate of Cs–137 on Volume Fractions Using the Cs–137 and Co–60 System

% ERROR IN COUNTRATE	ϵ_g	% error	ϵ_s	% error
+0.1	0.122	19	0.025	17
+0.5	0.013	91	0.0057	83
+1.0	-0.123	182	-0.021	170
+5.0	-1.170	893	-0.218	827
+10.0	-2.468	1745	-0.454	1613

Base Conditions: $\epsilon_g = 0.15$, $\epsilon_\ell = 0.82$, and $\epsilon_s = 0.03$

predicted gas holdup values. It is obvious from these results, that in order to accurately measure individual volume fractions in a three–phase system, one must use a relatively low energy source (e.g. Americium–241) and a high energy source (e.g. Cobalt–60).

If a suitable low energy gamma source is not available, then a three–phase system may be treated as a two–phase system (i.e. treat the solid phase and the liquid phase as a single phase), provided the weight fractions of the solid and liquid phases are known. These quantities are needed to calculate the attenuation coefficient for the slurry (see Eq. 3.6),

$$\frac{\mu_{s\ell}}{\rho_{s\ell}} = \sum_i \frac{\mu_i}{\rho_i}\omega_i \qquad i = 1 \text{ to no. of components} \tag{3.30}$$

The volume fraction of the slurry may be calculated using (see Eq. 3.10),

$$\epsilon_{s\ell} = \frac{-\ln(B / B_o)}{d\mu_{s\ell}} \tag{3.31}$$

where $\epsilon_{s\ell} = \epsilon_s + \epsilon_\ell$.

Experimental Apparatus and Operating Conditions

During some of the experiments in the 0.21 m ID column, the dual energy nuclear density gauge was used to determine gas holdups at various radial and axial locations. The density gauge system was composed of a movable assembly mechanism (MAM) which was used to transport the gauge both axially and radially along the column, two radioactive sources, two NaI detectors, and the associated electronics.

Movable Assembly Mechanism (MAM)

The MAM is used to transport the nuclear density gauges both axially and radially along the column. It is divided into two main parts, the axial movement mechanism (Figure 3.6) and the radial movement mechanism (Figure 3.7). Separate axial and radial movement mechanisms for the sources and detectors were constructed. Each axial movement mechanism consisted of a 6.35 cm diameter ball screw (Saginaw),

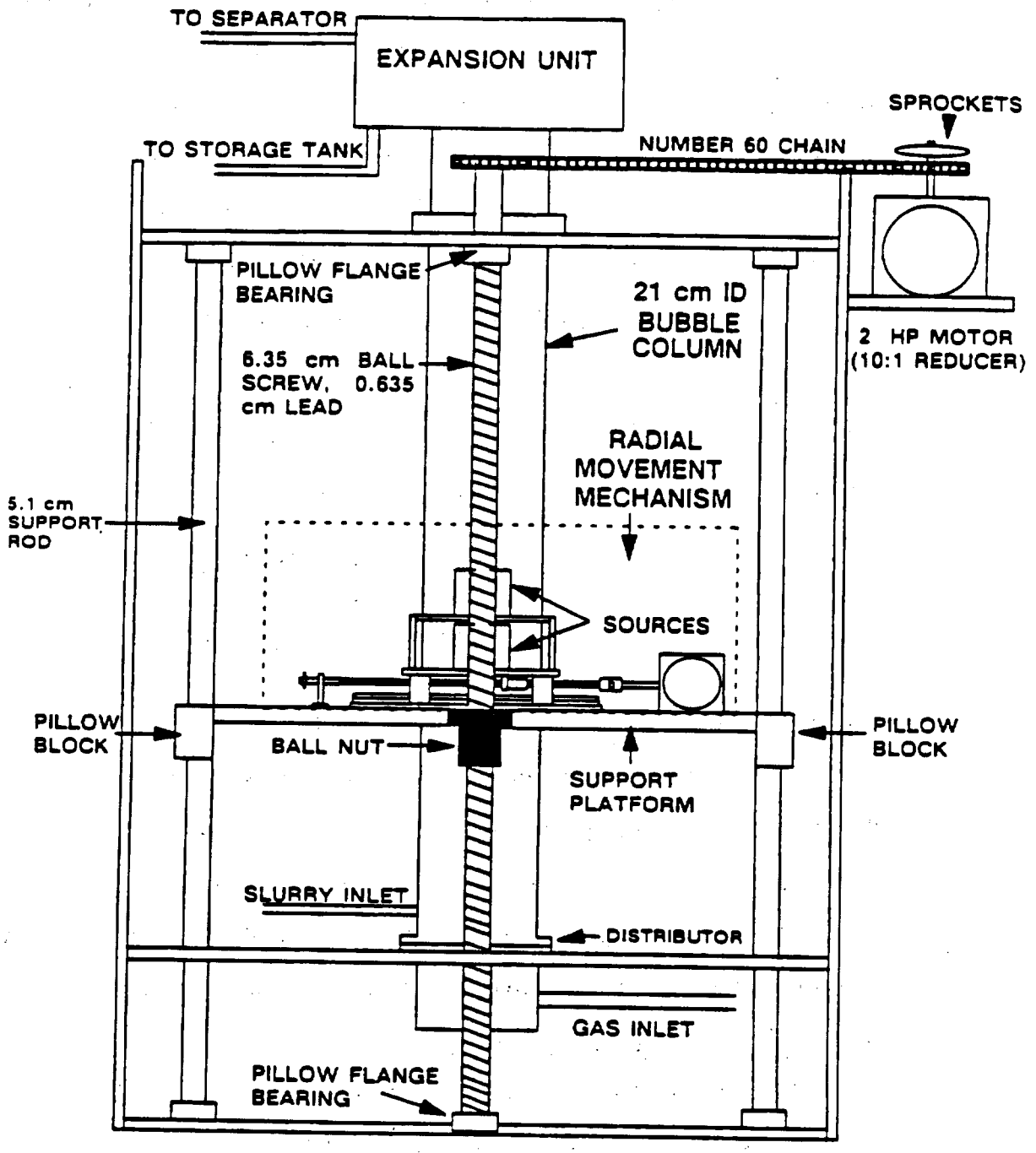

Figure 3.6. Schematic diagram of axial movement mechanism for the nuclear density gauge apparatus.

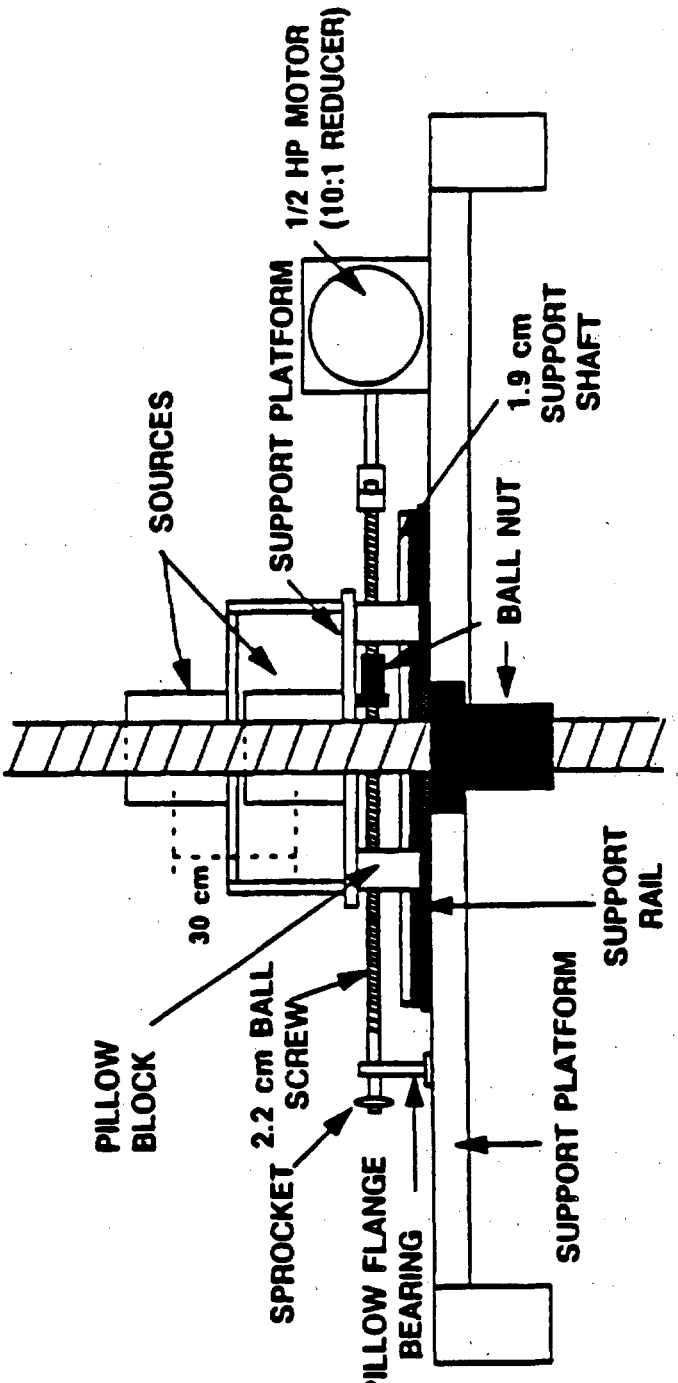

Figure 3.7. Schematic diagram of the radial movement mechanism for the nuclear density gauge apparatus.

3.3 m long, two support rods (5.1 cm diameter, 3.17 m long solids steel shafts), two 5.1 cm pillow blocks (Saginaw, SPB–32-ADJ), one non–preloaded ball nut (Saginaw, 5703263), two pillow flange bearings (Dodge, 059076), and one 1.27 cm thick aluminum plate on which the radial movement mechanism, was mounted. A 2 HP motor (Reliance, T16#3030) equipped with a 10:1 Tygear reducer (MR94667) and double single sprocket was mounted at the top of the apparatus and was used to transport the density gauge axially.

The radial movement mechanism was located on top of the aluminum plate described above (see Figure 3.7). Each radial movement mechanism consisted of two support shafts (1.9 cm diameter, 0.61 m long) which were mounted to two support rails (Saginaw, SR–12–PD), four pillow blocks (Saginaw, SPB–12–OPN), one ball screw 2.2 cm in diameter and 0.66 m long (Saginaw), one ball nut (Saginaw, 5708277), two pillow flange bearings (Dodge), and two 1.27 cm thick aluminum plates which supported the detectors or sources. A 1/4 HP motor (Reliance, T56H1019) equipped with a 10:1 Tygear reducer (MR94751) was mounted directly to the ball screw used to transport the sources radially. A chain and associated sprockets connected the radial movement mechanisms for the sources and detectors.

A series of magnetic switches were used to position the density gauge at predetermined locations (both axial and radial). The magnetic switches were connected to the motors and once activated, would turn–off the motor. Thus, measurements were made at the same location each time. This is extremely important for radial measurements, since the distance through the pipe varies with the radial position.

Sources and Detectors

A 35 mCi Cobalt–60 source, a 50 mCi Cesium–137 source, and a 300 mCi Americium – 241 source were used throughout our studies. The Cs–137 and Am–241 sources were donated by the Department of Energy and were previously used by Scientific

Applications Incorporated. The Cs–137 source was an encapsulated ceramic cylinder mm in diameter and 3 mm long. The Co–60 source was an encapsulated metal cylinder of Cobalt–60, 1 mm by 1 mm. Am–241 was a disc source measuring approximately 12 mm in diameter. The Am–241 source was tested in our system by placing it in a source holder without any collimation and using a NaI (sodium iodide) detector (1.5" diameter crystal, 1 mm thick) with a beryllium window. The column was filled with water and air was bubbled through. The count rate measured at the detector was approximately 150 counts/sec. Once collimated, the count rate would be substantially lower. We consulted various manufacturers about low energy gamma sources; however, we were unable to locate a point source with sufficient activity for our application. The strongest low energy gamma source we were able to locate was a 5 Ci Am–241 disc source with an effective diameter of 40 mm. However, once collimated with a 2.54 cm long collimator, 0.63 cm in diameter, the estimated count rate would be approximately 30 counts/sec. One other alternative available was to have a low energy source manufactured whi consisted of several disc or cylindrical sources aligned in series. Amersham makes a 25 Ci Am–241 source measuring 85 mm in length and 40 mm in diameter. If this source was used, we could expect a count rate of approximately 150 counts/sec, which is still extremely low. For dynamic systems, where the volume fraction of the individual phases at a given location fluctuate with time, higher count rates are required because the response time of the ratemeter is a function of the count rate. For a count rate of 150 counts/sec, it takes approximately 20 seconds (our system) for the count rate from the ratemeter to reach 99 % of its actual value. Thus, if count rates are measured over a short period of time, it is possible that they will not reflect the true (or average) count rate. Since, we were unable to obtain a low energy gamma source, we decided to use the Co–60 source and Cs–137 source as our two sources. We did not expect to obtain good results for three–phase measurements using this system (based on the discussion

presented in the section entitled Source Selection and Sensitivity Analysis); however, we felt we could always treat our three–phase system as a two–phase system using the measured weight fraction of solids (see Chapter II) to calculate a mean attenuation coefficient for the slurry.

The two source holders used to house the Co–60 and Cs–137 sources during measurements are shown in Figures 3.8 and 3.9, respectively. The Cobalt–60 source was collimated through a 76 mm long opening 5.1 mm in diameter and the Cesium source was collimated through a 50.8 mm long opening 6.35 mm in diameter. The source holders were designed such that the level of radiation detected at approximately 2 feet from the source (not including the open end) was less than 0.4 mrem/h.

NaI detectors (3.81 mm crystal diameter, 3.81 mm thick) manufactured by Bicron corporation were used with both the Co–60 source and Cs–137 source. The detectors were placed in an aluminum housings equipped with cooling coils (see Figure 3.10). A thermocouple was attached to the wall of the housing to monitor changes in the detector temperature. Collimators were also placed at the front of each detector and were approximately 38 mm long with a diameter of 6.35 mm.

Nuclear Electronics

A separate set of nuclear electronic components were used for each source–detector system so that data could be acquired simultaneously from both detectors. All nuclear electronics were manufactured by Tennelec and are listed in Table 3.4. Figure 3.11 is a schematic representation of the nuclear density gauge including the source, detector, electronics, and data acquisition system. The data acquisition system was the same as that used for acquiring data from the pressure transducers. The individual gamma pulses are amplified by the preamplifier, shaped and further amplified by an amplifier. Pulses from the amplifier pass through the single channel analyzer (SCA) which discriminates between different pulses so that only pulses corresponding to a given energy level are

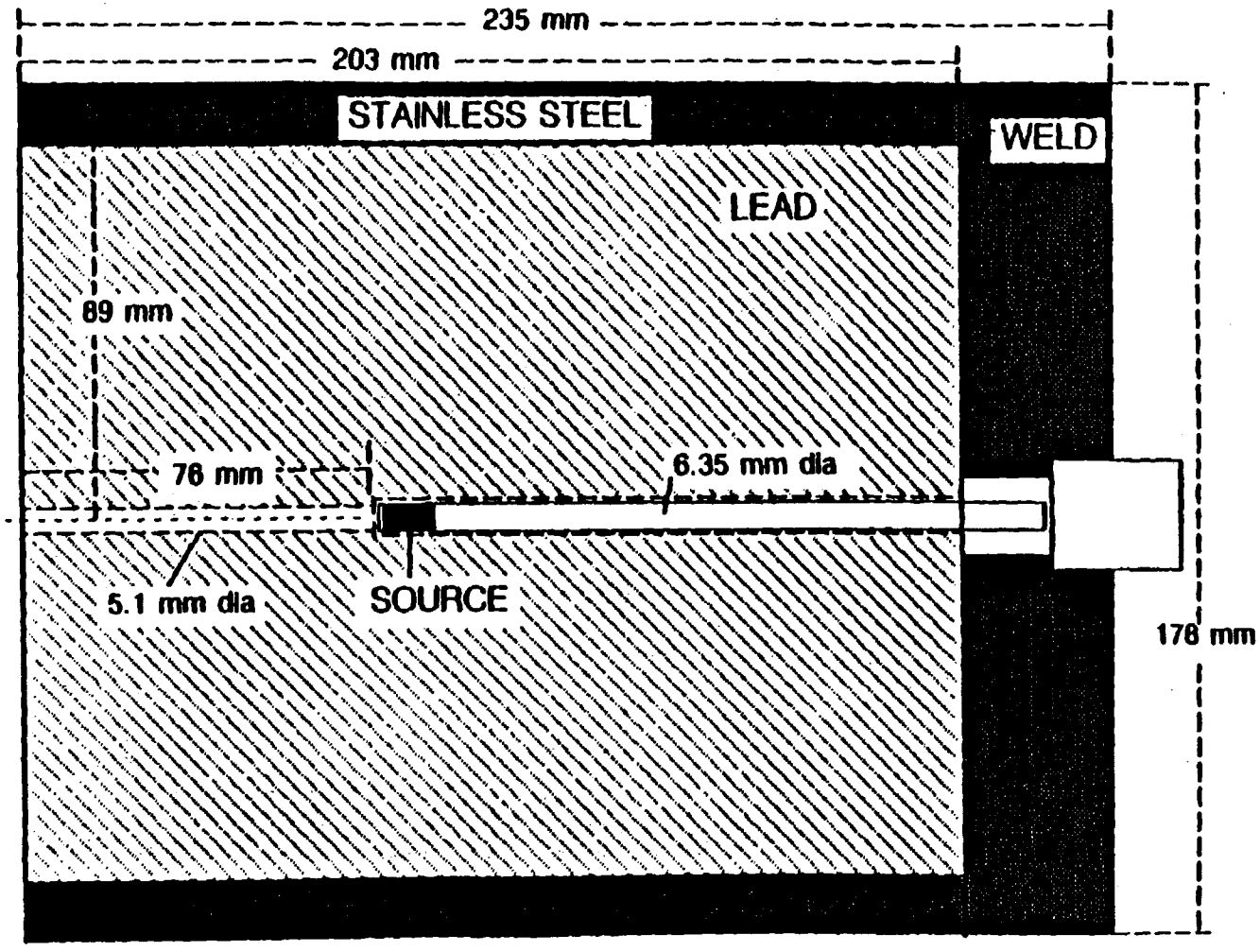

Figure 3.8. Schematic representation of . . Cobalt-60 source holder.

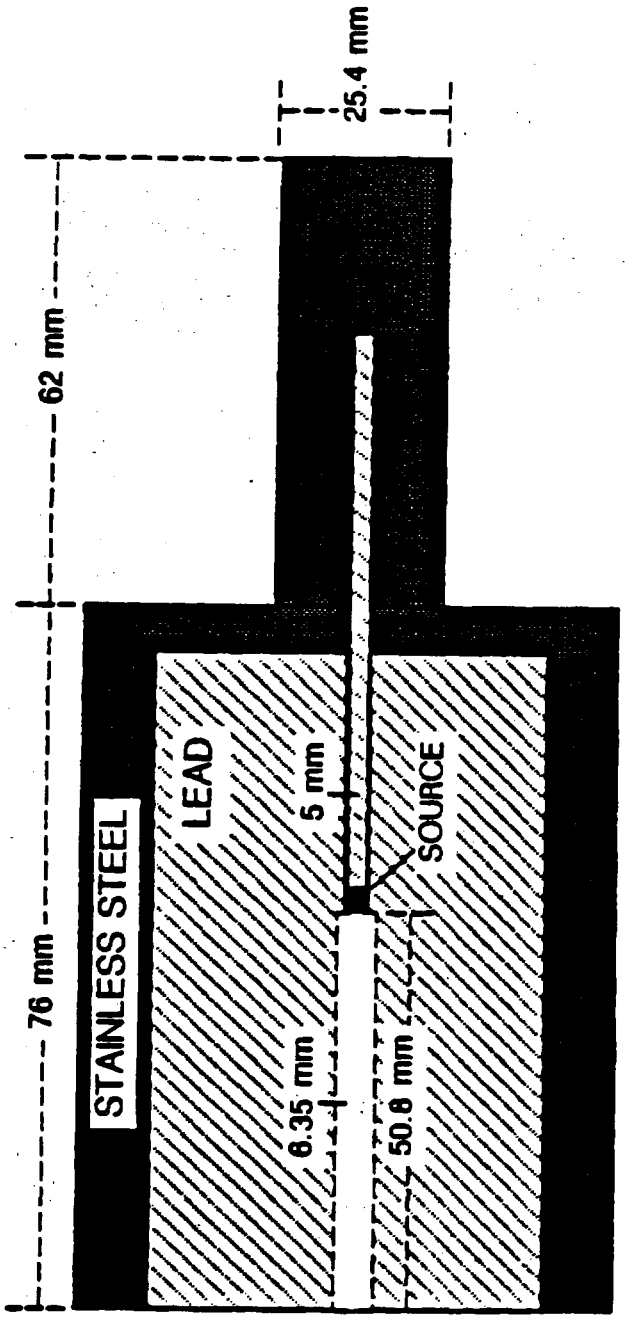

Figure 3.9. Schematic representation of the Ceslum-137 source holder.

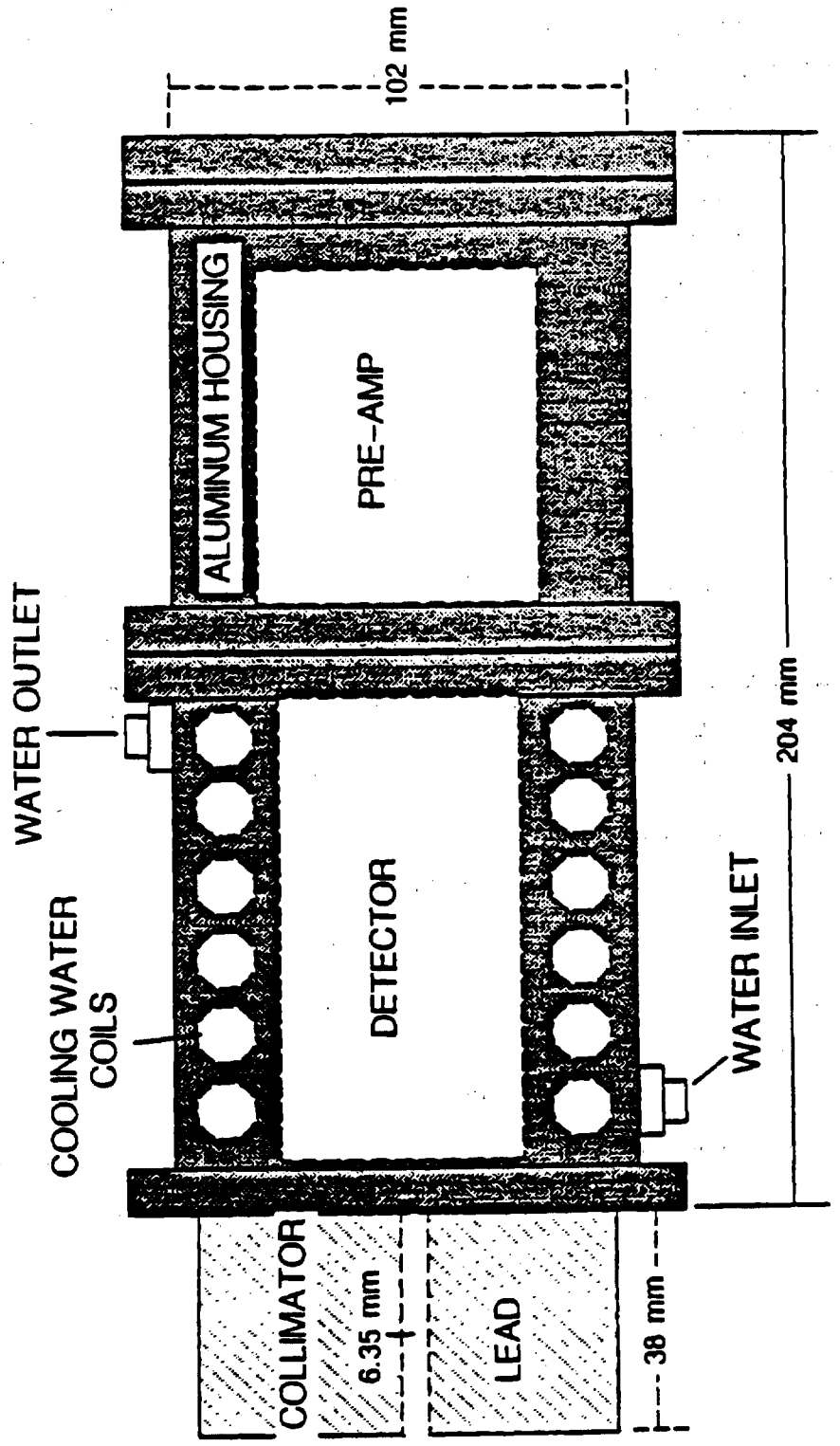

Figure 3.10. Schematic representation of the detector housing for the Cobalt-60 and Cesium-137 sources.

Table 3.4. Summary of Nuclear Density Gauge Electronics

EQUIPMENT	MANUFACTURER	MODEL #
DETECTOR	BICRON	1.5M1.5/1.5
HIGH VOLTAGE SUPPLY	TENNELEC	TC-948
PRE-AMPLIFIER	TENNELEC	TC-154A
AMPLIFIER	TENNELEC	TC-248
SCA[a]	TENNELEC	TC-450
RATEMETER	TENNELEC	TC-526

[a] SCA: Single channel analyzer

Table 3.5. Summary of Settings for the High Voltage Supply (HVS), Amplifier (AMP), and Single Channel Analyzer (SCA)

INSTRUMENT	DIAL	Co-60	Cs-137
HV	OUTPUT VOLTAGE	681	585
AMP	COARSE GAIN	100	50
	FINE GAIN	1.17	0.57
	TIMING AMP GAIN	50	50
SCA	UPPER LEVEL	9.5	5.0
	LOWER LEVEL	5.1	4.5

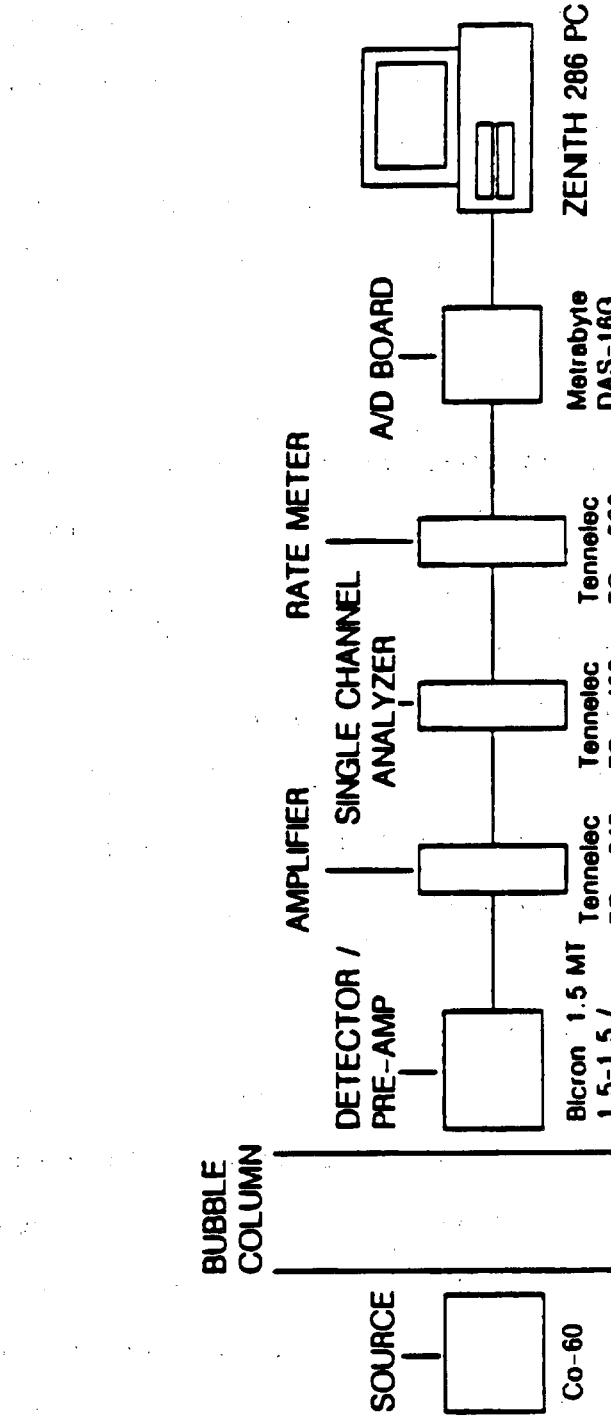

Figure 3.11. Schematic diagram of the nuclear density gauge electronic and data acquisition system.

counted. The output pulses from the SCA are then fed into the ratemeter and a voltage corresponding to the count rate is sent to the computer for data acquisition.

The single channel analyzers were operated in the normal mode of operation. Since we did not have access to a multichannel analyzer, the windows (i.e. lower level thresholds and upper level thresholds) were set experimentally using the procedure outlined in the SCA manual provided by Tennelec. The settings of the SCA as well as the other instrumentation is given in Table 3.5.

Calibration Procedures

Once the electronics were adjusted, calibration procedures were initiated to obtain attenuation coefficients for SASOL wax, FT-300 wax, iron oxide, and silica. A 0.1524 m wide x .1524 m deep x 0.61 m tall stainless steel chamber was constructed for conducting calibrations (see Figure 3.12). Attenuation coefficients were determined for wax at 265 ° C. In order to obtain the attenuation coefficient for pure wax (i.e. no solids), two measurements were made: (1) empty chamber, B_o and (2) full chamber, B. Knowing B, Bo and the thickness of the absorbing medium, d (i.e. 0.1524 m) the attenuation coefficient for the liquid phase was calculated using:

$$\mu_\ell = \frac{\ln(B / B_o)}{-d} \tag{3.32}$$

The attenuation coefficients for the solids (i.e. iron oxide and silica) could not be measured using the same procedure (i.e. filling the calibration chamber with pure solids) since voids exist between the individual solid particles. Due to the presence of the voids, the exact width of the absorbing medium is not known. To overcome this problem, a slurry composed of wax and solids was used to acquire the attenuation coefficients of the solids. First, an empty chamber count rate, B_o was obtained. Then, a known amount of wax was added to the calibration chamber and heated to 265 °C. Once at temperature, solids were added to form a 10 wt % slurry. A stirrer was used to

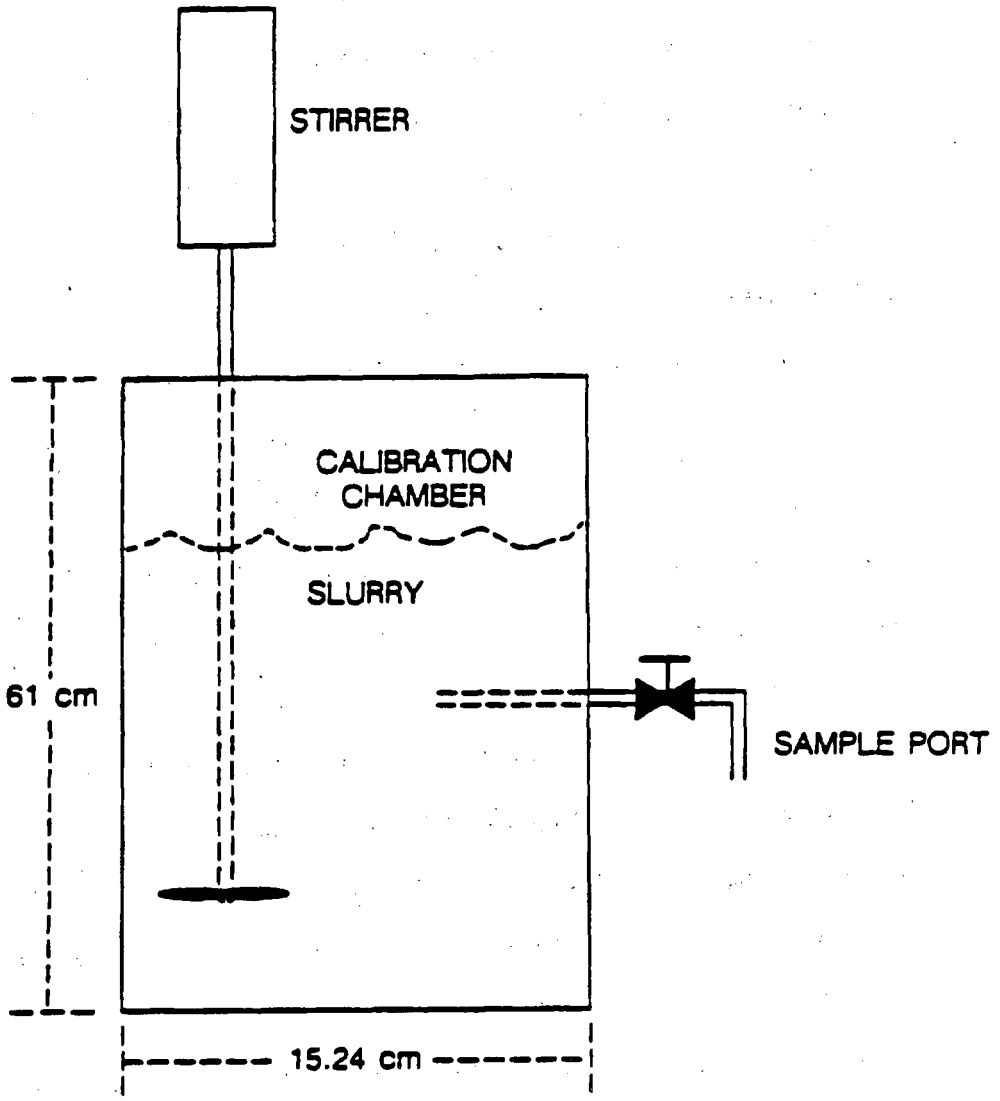

Figure 3.12. Schematic diagram of the calibration chamber.

suspend the solid particles. Once the system stabilized (approximately 30 minutes) a full chamber count rate, B was obtained, and a sample of the slurry was withdrawn at the same height at which the measurement was made and analyzed (using the procedure described in Chapter II) to determine the solids concentration in the slurry. The solids concentrations from the samples were within 3% (relative) of the solids concentrations calculated based on the amount of wax and solids added to the chamber. B, B_o, μ_ℓ, and the measured solids weight fraction were then used to calculate the attenuation coefficient for the solid phase (i.e. iron oxide or silica) using:

$$\mu_s = \frac{\frac{\ln(B/B_o)}{-d} - \frac{(1-\omega_s)\rho_{sl}\mu_l}{\rho_l}}{\frac{\omega_s \rho_{sl}}{\rho_s}} \qquad (3.33)$$

This procedure was repeated with solids concentrations of 20 and 30 wt% for each solid type, and the average attenuation coefficient from the three measurements was used in subsequent calculations. Table 3.6 lists the measured attenuation coefficients for SASOL wax and FT–300 wax. Also shown in Table 3.6 is the measured attenuation coefficients for iron oxide and silica using 10, 20, and 30 wt% slurries, as well as the average values of the attenuation coefficient for each solid. There was very good agreement between attenuation coefficients obtained using different slurry concentrations.

Table 3.7 compares the measured attenuation coefficients to those calculated based on the data presented by Attix (1968) (see Table 3.1). Their is very good agreement between the measured and predicted attenuation coefficients.

Data Acquisition and Reduction Procedures

Nuclear density gauge measurements were made during the majority of experiments in the 0.21 m ID stainless steel column. As mentioned previously (see Chapter II), during experiments the system was allowed to remain at a given set of conditions (i.e. constant gas flow rate) for a period of one and a half hours. Measurements with the

Table 3.6. Measured Attenuation Coefficients (cm^{-1}) for FT-300 Wax, SASOL Wax, Iron Oxide, and Silica

ABSORBING MEDIUM	WT% SOLIDS	SOURCE	
		Co-60	Cs-137
FT-300 WAX	-	0.0421	0.0555
SASOL WAX	-	0.0415	0.0519
IRON OXIDE	10	0.2718	0.3910
	20	0.2690	0.3891
	30	0.2750	0.3920
SILICA	10	0.1411	0.2039
	20	0.1409	0.2072
	30	0.1380	0.2110
IRON OXIDE	AVERAGE	0.272	0.391
SILICA	AVERAGE	0.140	0.207

Table 3.7. Comparison of Measured and Theoretical Attenuation Coefficients (cm^{-1})

ABSORBING MEDIUM	Co-60		Cs-137	
	Measured	Theoretical	Measured	Theoretical
FT-300 WAX	0.0421	0.0423	0.0555	0.0580
IRON OXIDE	0.272	0.271	0.391	0.382
SILICA	0.140	0.148	0.207	0.205

nuclear density gauge were initiated after approximately one hour. The output voltage from the ratemeter is related to the count rate through a scaling factor, S_C. For all measurements, S_C was 500. The count rate at time i is calculated from the output voltage using the following expression

$$B_i = (\text{OutputVoltage})_i(S_C) \tag{3.34}$$

Count rates were determined from output voltage data recorded over a period of 2 to 3 minutes at a sampling frequency of 50 Hz using the data acquisition system described in Chapter II. The output voltages at each time, were converted to count rates via Eq. 3.34, and the average count rate, B, which was used in all calculations is

$$B = \frac{\sum_i^n B_i}{n} \tag{3.35}$$

where n is the total number of data points (e.g. if one samples at 50 Hz for 60 seconds, n would be 3000). The average count rate was used to determine the phase fractions in the system. Figure 3.13 is a schematic representation of the locations at which measurements were made. In some experiments, measurements were limited to heights of 0.91 and 1.52 m above the distributor. The distance through the column, which represents the thickness of the absorbing media, at each measurement location was measured experimentally by obtaining count rates for the empty column at each position and count rates with a full column of wax (i.e. no gas) at each position. These values, together with the attenuation coefficient for wax were used to calculate the distance through the column at each location using,

$$d_i = \frac{\ln(B_i / B_{o_i})}{-\mu_\ell} \tag{3.36}$$

where i represents the location of the density gauge (see Figure 3.13). Values of d_i were obtained at the beginning of each set (or batch) of experiments. These values

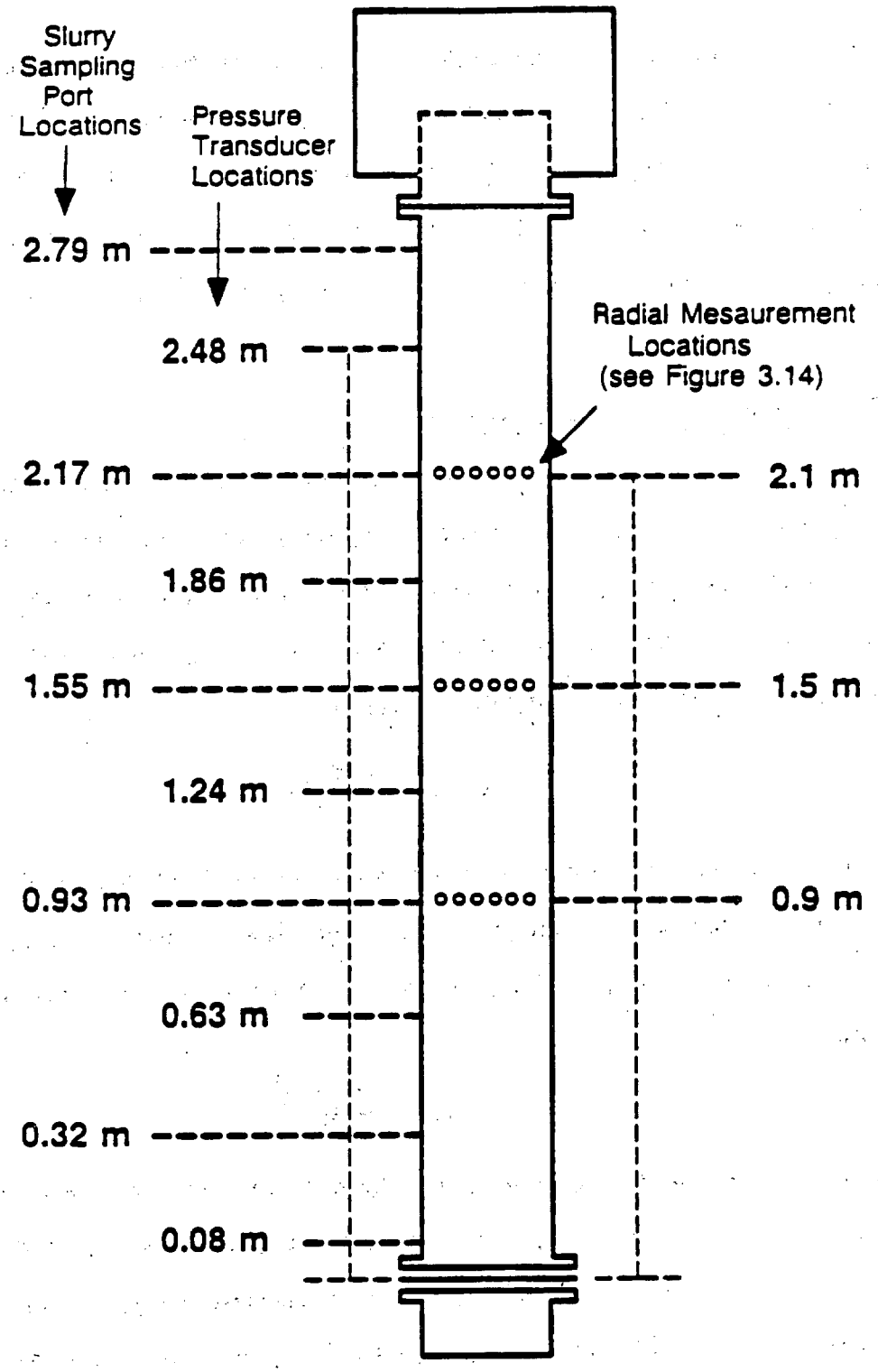

Figure 3.13. Schematic diagram of the nuclear density gauge measurement locations.